Structural insights into the transport and gating mechanisms of the plant high-affinity K^+ transporter AtHAK5

Chu Wang[1,2,3,4,6], Xiaohui Wang[5,6,*], Yannan Qu[2,3,4] and Huaizong Shen[2,3,4,*]

[1]Fudan University, Shanghai, China

[2]Zhejiang Key Laboratory of Structural Biology, School of Life Sciences, Westlake University, Hangzhou, Zhejiang, China

[3]Westlake Laboratory of Life Sciences and Biomedicine, Hangzhou, Zhejiang, China

[4]Institute of Biology, Westlake Institute for Advanced Study, Hangzhou, Zhejiang, China

[5]Key Laboratory of Systems Health Science of Zhejiang Province, School of Life Science, Hangzhou Institute for Advanced Study, University of Chinese Academy of Sciences, Hangzhou, Zhejiang, China

[6]These authors contributed equally to this work.

[*]To whom correspondence should be addressed: X. Wang (wangxiaohui@ucas.ac.cn); H. Shen (shenhuaizong@westlake.edu.cn).

Abstract

Plant high-affinity K^+ (HAK) transporters are essential for survival in nutrient-depleted soils. However, the mechanisms governing their energetically costly active transport and stringent regulation have remained structurally elusive. Here, we present high-resolution cryo-EM structures of *Arabidopsis thaliana* HAK5, revealing a homodimeric assembly characterized by a modified LeuT-fold. A unique topological "knot" within the permeation pathway establishes a selective K^+ coordination site and coordinates critical residues facilitating proton-coupled symport. Unexpectedly, we discovered a uniquely folded adenine nucleotide-binding domain (NBD) at the cytoplasmic interface. The bound endogenous ADP orients an intracellular loop (ICL_{gate}) to physically plug the intracellular exit of the pore. Crucially, structural analysis of rationally engineered nucleotide-binding mutants reveals a substantial rigid-body rearrangement of the cytoplasmic domain that displaces this plug to open the gate. Validated by *in vivo* yeast complementation assays, these structural insights unveil a sophisticated autoinhibitory mechanism that directly couples the mechanical gating of ion transport to the cellular energy status. This study provides a definitive structural framework for understanding plant HAK transporters and offers a crucial blueprint for engineering nutrient-efficient crops.

Introduction

Potassium (K^+) is an essential macronutrient for plants, constituting up to 10% of plant dry weight [1]. It plays indispensable roles in fundamental physiological processes, including enzyme activation, protein synthesis, stomatal regulation, turgor-driven cell expansion, and abiotic stress resilience [2,3]. In natural and agricultural environments, however, soil K^+ concentrations are highly dynamic and frequently drop to micromolar levels, severely limiting plant growth and crop yield [4-6]. To cope with fluctuating K^+ availability, plants have evolved sophisticated, dual-affinity root acquisition systems[7]. Root K^+ uptake is primarily mediated by two distinct mechanisms: the inward-rectifying K^+ channel AKT1, which dominates under K^+-sufficient conditions but thermodynamically fails at low concentrations, and the high-affinity transporters of the HAK/KUP/KT (high-affinity K^+ transporters/K^+ uptake permeases/K^+ transporters) family, which become critical under severe K^+ limitation[8,9].

Among the HAK/KUP/KT family members, *Arabidopsis thaliana* HAK5 (AtHAK5) is the primary contributor to root high-affinity K^+ acquisition when external concentrations fall below 20 μM[10,11]. Operating as an active K^+/H^+ symporter, AtHAK5 couples the energetically demanding uphill transport of K^+ to the downhill flux of protons, utilizing the plasma membrane proton motive force[12]. Because active K^+ uptake against steep concentration gradients exacts a high metabolic cost, the activity of HAK5 is stringently regulated[13,14]. Under K^+ deprivation, *AtHAK5* transcription is strongly upregulated[15], and its transport activity is rapidly enhanced post-translationally via phosphorylation by the CBL-CIPK network (e.g., the CBL1/9-CIPK23 complex)[16].

Furthermore, recent physiological evidence suggests that HAK5 function must be intimately linked to the cellular energy status to prevent energy depletion during stress[17]; yet, the molecular basis of this intricate gating and regulatory logic has remained largely unknown.

Despite the profound physiological importance of HAK5-mediated K^+ uptake, the structural biology of plant HAK/KUP/KT transporters has remained elusive[18]. To date, mechanistic insights into HAK transporters have predominantly relied on mutational studies and homology modeling based on a distantly related bacterial ortholog, *Bacillus subtilis* KimA (BsKimA)[19]. However, these prokaryotic models lack the extended, highly divergent cytoplasmic N- and C-terminal domains found in plant HAKs, which are known to be essential for eukaryotic sensing, autoinhibition, and regulation[16]. Consequently, the precise architecture of the ion permeation pathway, the structural basis of high-affinity K^+ coordination, and the mechanisms underlying proton coupling and energy-dependent transport gating in higher plants have remained entirely unresolved.

Here, we present a series of high-resolution cryogenic electron microscopy (cryo-EM) structures of AtHAK5. These structures unveil its dimeric assembly, the complete ion permeation pathway and coordination site, the proton-coupling network, and a novel cytoplasmic adenine nucleotide-binding domain. This work bridges a critical gap in plant transporter structural biology, defines an energy-dependent regulatory paradigm, and provides a framework for engineering crops with enhanced K^+-use efficiency.

Results

Structural determination and homodimeric architecture of AtHAK5

To elucidate the molecular basis of high-affinity potassium uptake, full-length AtHAK5 (UniProt ID: Q9M7K4) (Supplemental Figure S1) was N-terminally FLAG- and GFP-tagged, recombinantly expressed in HEK293 cells, and purified using affinity and size-exclusion chromatography (SEC) (Supplemental Figure S1A, B). From the peak SEC fractions, we successfully reconstructed the AtHAK5 cryo-EM density map to an overall resolution of 2.66 Å (Figure 1A, B and Supplemental Figure S2C). The exceptional quality of the map enabled unambiguous *de novo* atomic modeling of the majority of the protein, including the transmembrane (TM) helices, the extended intracellular domains, and the coordinated K^+ and ADP ligands (Figure 1C, Supplemental Figure S3-5 and Table S1). The extreme N-terminus (residues 1–55) and two cytosolic loops (residues 161–166 and 655–715) were invisible in the map, reflecting their intrinsic flexibility.

Like its prokaryotic homolog BsKimA, AtHAK5 adopts a symmetric homodimeric architecture (Figure 1C and Supplemental Figure S6A). Intriguingly, the dimeric interface is mediated exclusively by the massive cytoplasmic domains. Yeast complementation assays revealed that dimer-disruptive mutations at this interface (L581E and L777E) do not impair K^+ absorption (Supplemental Figure S6B, C), suggesting that individual protomers can function independently. Furthermore, unlike BsKimA, which exhibits a domain-swapped configuration between the TM and cytoplasmic domains, the TM and cytoplasmic regions of each AtHAK5 protomer associate strictly in *cis*, forming extensive intra-protomer interactions (Figure 1C).

Within each protomer, the membrane-spanning region comprises twelve TM helices (Figure 1D). Strikingly, TM1 through TM10 fold into a highly conserved inverted-topology repeat characteristic of the LeuT-fold superfamily[20-23], with TM1–TM5 and TM6–TM10 operating as pseudo-symmetrical halves (Figure 1E). TMs 11 and 12 pack loosely against the periphery of this core, with TM12 protruding deeply into the cytoplasmic space. Viewed from the extracellular face, TM1, TM3, TM6, and TM8—with contributions from TM10—converge to form a distinctive structural "knot" (Figure 1E). This topological arrangement intimately shapes the central ion permeation pathway.

Molecular basis of high-affinity K^+ coordination

Deep within the central cavity enclosed by this structural knot, we identified a strong, non-protein density (Figure 2A and Supplemental Figure S4). Given the high selectivity for K^+ and the use of 150 mM KCl (without Na^+) during purification, we modeled a K^+ ion into this density. The high-resolution map allowed us to pinpoint a stringent K^+ coordination site uniquely tailored to dehydrate and anchor the ion. The K^+ is coordinated by a tight cluster of polar and charged residues: D72, S76, and Y79 on TM1; T309 on TM6; and Y450 on TM10 (Figure 2A). Additionally, a conserved Leu306 is positioned directly above the coordination site, presumably acting as an extracellular lid gating ion entry. Notably, the ^{67}GVVYGD^{72} motif on TM1, which is strictly conserved across plant HAK transporters but absent in bacterial BsKimA, exhibits structural homology with the canonical T(V/I)GYGD selectivity filter of K^+ channels[9,24,25], revealing a fascinating convergent evolutionary relationship between plant HAKs and K^+ channels.

136

137 To validate the physiological indispensability of this structural geometry, we
138 performed *in vivo* complementation assays using the *Saccharomyces cerevisiae* strain
139 CY162 (R5421). This K^+-uptake deficient strain is unable to survive on K^+-depleted media,
140 making it an ideal system for assessing high-affinity transport. While wild-type AtHAK5
141 robustly restored yeast growth on strictly limiting media (0.1 mM K^+), single point
142 mutations disrupting the primary K^+ coordination sphere (D72A, Y79A, T309A, and
143 Y450A) severely impaired or completely abolished complementation (Figure 2B). The
144 L306F mutation also dramatically impaired growth, likely by sterically blocking the
145 extracellular entrance. These functional data perfectly corroborate the structural model,
146 confirming that this precise architecture dictates high-affinity ion selectivity.

147

148 **A cytoplasmic loop autoinhibits intracellular ion release**

149 Surface analysis of the ion permeation pathway reveals that the pore narrows to a radius of
150 less than 1 Å beneath the K^+ binding site, indicating that the captured structure represents
151 an intracellularly occluded state (Figure 3A, B). The intracellular exit is structurally
152 constricted by a tight cluster of residues including D123, E126, F130, S134, and Q397
153 (Figure 3C). Strikingly, this exit is physically plugged by a specific regulatory loop
154 extending from the cytoplasmic domain (designated ICL_{gate}, connecting β6 and α3). The tip
155 of ICL_{gate} harbors Y628 and K629, which project directly into the intracellular vestibule,
156 forming extensive interactions with the exit-lining residues (particularly F130) to firmly
157 obstruct the pore (Figure 3C). Furthermore, residues N599 and R600, located on a separate

158 cytosolic loop connecting β4 and β5, buttress and stabilize the ICL_{gate} in this occluded
159 conformation.
160
161 We tested this structural observation using yeast complementation. Disrupting this
162 physical "plug" via targeted mutations (Y628A/K629A or Y628D/K629D), or mutating its
163 key interacting partner on TM3 (F130S), yielded distinctly hyperactive transport
164 phenotypes, uncoupling the transporter from its native inhibition (Figure 3D). This
165 perfectly aligns with previous physiological research identifying that the F130S mutation
166 enhances AtHAK5 K^+ affinity by over 100-fold[26,27]. Consistent with their critical functions,
167 both F130 and Y628 are strictly conserved across plant HAK transporters (Supplemental
168 Figure S1). Together, these data demonstrate that the ICL_{gate} acts as a mechanical
169 autoinhibitory plug.
170
171 **Discovery of a novel cytoplasmic adenine nucleotide-binding domain**
172 A long-standing enigma regarding plant HAK transporters has been the function of their
173 massive cytoplasmic domains. Remarkably, our cryo-EM map resolved a well-ordered,
174 distinctively folded domain composed of β-strands and α-helices at the cytoplasmic
175 interface (Figure 1C, D and Supplemental Figure S3). Deep within a highly basic pocket of
176 this domain, the electron density perfectly matched an endogenous ADP molecule. The
177 ADP is anchored by residues R406, H527, K530, E565, T735, Y755, K759, and L769
178 (Figure 4A, B), where the positively charged residues coordinate the phosphates, and the
179 negatively charged E565 stabilizes the adenine base. Exhaustive structural searches using

Foldseek and Dali returned no homologous folds outside the HAK family, identifying this nucleotide-binding domain (NBD) as a novel structural fold.

Given the spatial capacity of the binding pocket, we hypothesized it could accommodate ATP, and that an ATP-bound state might relieve the autoinhibition observed in the ADP-bound structure. Despite extensive biochemical attempts to capture an ATP-bound open state via ADP displacement (utilizing extended dialysis, AMPPNP incubation, or NaCl buffer substitution), subsequent cryo-EM analyses revealed no global conformational changes (RMSD < 0.7 Å compared to WT) (Supplemental Figure S7 and S8 and Table S1). However, localized electron density variations beyond the β-phosphate in the dialyzed-ATP and NaCl+ATP datasets hinted at partial ADP-to-ATP exchange (Supplemental Figure S9), suggesting the open state may be highly transient or requires additional cellular factors.

To investigate the regulatory role of the NBD, we performed yeast complementation assays on the nucleotide-coordinating residues, which revealed strikingly divergent functional consequences. While mutations H527A, E565A, and R406A abrogated transport activity, the mutations K530A, T735A, Y755A, K759A, and L769A dramatically enhanced it, supporting robust yeast growth even without added K^+ (0 mM) (Figure 4C). We rationalize this dichotomy structurally: the activity-abrogating mutations likely cause severe local misfolding preventing any nucleotide binding, whereas the activity-enhancing mutations subtly destabilize the autoinhibitory ADP-bound state. We subsequently determined the structures of AtHAK5(H527A) (inhibited) and AtHAK5(K759A)

(hyperactive) (Supplemental Figure S7 and S8 and Table S1). While both maintained the overall WT fold (RMSD < 0.35 Å), both exhibited significantly weakened density at the α-phosphate region, confirming impaired ADP binding dynamics (Supplemental Figure S9).

The NBD structurally regulates the autoinhibitory ICL_{gate}

To further decode how the NBD regulates transport, we performed a comprehensive sequence alignment of the NBD across various plant HAK homologs (Figure 5A). This analysis revealed two distinct evolutionary clades: one represented by AtHAK5, featuring conserved H527, E565, E734, K759, and K778; and another represented by ZmHAK4[28], which naturally substitutes these positions with Arg, Asn, Lys, His, and Glu, respectively (Figure 5B and Supplemental Figure S1).

Hypothesizing that these divergent sequences represent distinct set-points for energy-dependent gating, we engineered AtHAK5 mutants by systematically swapping key ADP-interacting residues with their ZmHAK4-clade counterparts. Yeast complementation revealed that, with the exception of the E565N single mutant, these ZmHAK4-like single, double (H527R/K759H, designated AtHAK5-M2), triple (H527R/E565N/K759H, designated AtHAK5-M3), and quintuple (H527R/E565N/E734K/K759H/K778E, designated AtHAK5-M5) mutations dramatically promoted yeast growth, indicating constitutive hyperactivity (Figure 5C).

To uncover the structural basis of this hyperactivity, we determined the cryo-EM structures of the double (AtHAK5-M2), triple (AtHAK5-M3), and quintuple (AtHAK5-

M5) mutants (Supplemental Figure S7-10 and Table S1). While the double mutant remained in the autoinhibited WT-like conformation (Supplemental Figure S7), the triple and quintuple mutants captured a profound structural metamorphosis (Figure 5D and Supplemental Figure S7). The entire cytoplasmic NBD swung dramatically toward the dimeric interface, pivoting rigidly around the elongated TM12 helix. This massive rigid-body movement physically retracted the ICL_{gate} away from the TM core, completely unplugging the intracellular exit of the potassium permeation pathway. Analysis of the nucleotide pocket in these uninhibited states revealed altered local densities (Supplemental Figure S9), suggesting a restructuring of the pocket that potentially favors ATP binding.

Together, these structural and functional results demonstrate that the NBD acts as a mobile regulatory module. By rationally engineering the electrostatic and spatial configuration of the nucleotide-binding pocket, the NBD can be progressively decoupled from its autoinhibitory state, forcibly displacing the ICL_{gate} plug. This elegant mechanism allows the plant cell to directly couple the mechanical gating of high-affinity K^+ uptake to its intracellular energy landscape.

Discussion

The acquisition of potassium from severely depleted soils represents one of the most formidable challenges in plant mineral nutrition. While physiological studies have long established HAK5 as the primary engine for high-affinity K^+ uptake in roots, the molecular mechanics of this transporter have remained elusive. The high-resolution cryo-EM structures of AtHAK5 presented here resolve this long-standing enigma, unveiling a highly

sophisticated molecular machine that couples a canonical transport mechanism with an unprecedented, energy-sensing autoinhibitory gate.

A defining feature of the AtHAK5 architecture is its modified LeuT-fold, wherein the spatial convergence of TM1, TM3, TM6, TM8, and TM10 creates a distinctive structural "knot." This topological arrangement forms a highly selective K^+ coordination sphere that discriminates against highly abundant, competing cations like Na^+. Notably, the K^+-coordinating ^{67}GVVYGD^{72} motif on TM1 exhibits profound structural homology to the canonical T(V/I)GYGD selectivity filter found in classical K^+ channels[29,30]. Because plant HAKs and K^+ channels possess entirely distinct global folds and evolutionary origins, this structural mimicry represents a remarkable instance of convergent evolution, wherein nature has arrived at an optimal geometric solution for K^+ dehydration and coordination across distinct protein lineages.

However, the most profound discovery of this study is the identification of the cytoplasmic adenine nucleotide-binding domain (NBD) and its role as an autoinhibitory energy sensor. Because active K^+/H^+ symport is highly metabolically demanding, unchecked transport during periods of severe stress or nutrient starvation could lethally deplete cellular energy reserves. Our structures provide a definitive mechanical explanation for how plants prevent this: AtHAK5 functions not just as a transporter, but as a molecular rheostat. In the energy-depleted state, the binding of ADP to the NBD stabilizes a conformation in which the ICL_{gate} (anchored by Y628 and K629) physically plugs the intracellular exit of the permeation pathway, arresting transport.

The structural analyses of our rationally engineered, constitutively active ZmHAK4-like mutants powerfully illuminate the mechanism of transport relief. Upon alteration of the nucleotide-binding pocket—mimicking the transition to an uninhibited state—the entire NBD undergoes a massive rigid-body rotation, pivoting around the elongated TM12 helix. This mechanical lever effectively retracts the ICL_{gate} from the transmembrane core, unplugging the pore and permitting K^+ release into the cytosol. This elegantly simple, yet highly effective coupling of a soluble metabolic sensor to a transmembrane mechanical gate represents a novel regulatory paradigm in plant ion transport.

The evolutionary divergence of the NBD into two distinct clades—typified by AtHAK5 and ZmHAK4—suggests that different plant species have evolved distinct energetic "set-points" for K^+ uptake. Variations in the key nucleotide-coordinating residues likely dictate the relative affinity for ATP versus ADP, thereby tuning the transporter's responsiveness to the cellular energy charge according to the specific ecological niche or metabolic demands of the species. This natural variation offers a fascinating glimpse into the evolutionary adaptability of plant nutrient acquisition systems.

Ultimately, these structural and mechanistic insights hold profound implications for global agriculture. As soil degradation accelerates and the availability of viable agricultural land diminishes, the development of crops with enhanced nutrient-use efficiency is paramount[31]. The atomic-level blueprint of the AtHAK5 permeation pathway,

295 combined with the discovery of its tunable energy-sensing NBD, provides precise genetic
296 targets. By rationally engineering the NBD to bypass autoinhibition, or by optimizing the
297 proton-coupling for enhanced K^+ capture, it may be possible to design advanced crop
298 varieties capable of thriving in marginal, K^+-deficient soils without the heavy reliance on
299 costly and environmentally damaging fertilizers[32,33].
300

References

1 Ahmad, I. & Maathuis, F. J. Cellular and tissue distribution of potassium: physiological relevance, mechanisms and regulation. *J Plant Physiol* **171**, 708-714, doi:10.1016/j.jplph.2013.10.016 (2014).

2 Wang, M., Zheng, Q., Shen, Q. & Guo, S. The critical role of potassium in plant stress response. *Int J Mol Sci* **14**, 7370-7390, doi:10.3390/ijms14047370 (2013).

3 Anschutz, U., Becker, D. & Shabala, S. Going beyond nutrition: regulation of potassium homoeostasis as a common denominator of plant adaptive responses to environment. *J Plant Physiol* **171**, 670-687, doi:10.1016/j.jplph.2014.01.009 (2014).

4 Battie-Laclau, P. *et al.* Photosynthetic and anatomical responses of Eucalyptus grandis leaves to potassium and sodium supply in a field experiment. *Plant, cell & environment* **37**, 70-81, doi:10.1111/pce.12131 (2013).

5 Adams, E. & Shin, R. Transport, signaling, and homeostasis of potassium and sodium in plants. *Journal of Integrative Plant Biology* **56**, 231-249, doi:10.1111/jipb.12159 (2014).

6 Zorb, C., Senbayram, M. & Peiter, E. Potassium in agriculture--status and perspectives. *J Plant Physiol* **171**, 656-669, doi:10.1016/j.jplph.2013.08.008 (2014).

7 Coskun, D., Britto, D. T., Kochian, L. V. & Kronzucker, H. J. How high do ion fluxes go? A re-evaluation of the two-mechanism model of K(+) transport in plant roots. *Plant Sci* **243**, 96-104, doi:10.1016/j.plantsci.2015.12.003 (2016).

8 Dreyer, I. & Uozumi, N. Potassium channels in plant cells. *Febs j* **278**, 4293-4303, doi:10.1111/j.1742-4658.2011.08371.x (2011).

9 Durell, S. R., Hao, Y., Nakamura, T., Bakker, E. P. & Guy, H. R. Evolutionary relationship between K(+) channels and symporters. *Biophys J* **77**, 775-788, doi:10.1016/s0006-3495(99)76931-6 (1999).

10 Gierth, M., Mäser, P. & Schroeder, J. I. The Potassium Transporter AtHAK5 Functions in K^+ Deprivation-Induced High-Affinity K^+ Uptake and AKT1 K^+ Channel Contribution to K^+ Uptake Kinetics in Arabidopsis Roots. *Plant Physiology* **137**, 1105-1114, doi:10.1104/pp.104.057216 (2005).

11 Qi, Z. *et al.* The high affinity K^+ transporter AtHAK5 plays a physiological role in planta at very low K^+ concentrations and provides a caesium uptake pathway in *Arabidopsis*. *J Exp Bot* **59**, 595-607, doi:10.1093/jxb/erm330 (2008).

12 Rubio, F., Nieves-Cordones, M., Alemán, F. & Martínez, V. Relative contribution of AtHAK5 and AtAKT1 to K^+ uptake in the high-affinity range of concentrations. *Physiologia Plantarum* **134**, 598-608, doi:10.1111/j.1399-3054.2008.01168.x (2008).

13 Ta, N. *et al.* Identification of Functional Sites of High-Affinity HAK5 *SCIENTIA SINICA Vitae* **44**, 929-937, doi:10.1360/n052014-00088 (2014).

14 Nieves-Cordones, M., Alemán, F., Martínez, V. & Rubio, F. K^+ uptake in plant roots. The systems involved, their regulation and parallels in other organisms. *Journal of Plant Physiology* **171**, 688-695, doi:10.1016/j.jplph.2013.09.021 (2014).

15 Lara, A. *et al.* Arabidopsis K+ transporter HAK5-mediated high-affinity root K+ uptake is regulated by protein kinases CIPK1 and CIPK9. *Journal of Experimental Botany* **71**, 5053-5060, doi:10.1093/jxb/eraa212 (2020).

16 Ródenas, R. *et al.* Insights into the mechanisms of transport and regulation of the arabidopsis high-affinity K^+ transporter HAK51. *Plant Physiology* **185**, 1860-1874, doi:10.1093/plphys/kiab028 (2021).

17 Nieves-Cordones, M., Alemán, F., Fon, M., Martínez, V. & Rubio, F. in *Environmental Adaptations and Stress Tolerance of Plants in the Era of Climate Change* 85-112 (Springer New York, 2012).

18 Cai, K., Zeng, F., Wang, J. & Zhang, G. Identification and characterization of HAK/KUP/KT potassium transporter gene family in barley and their expression under abiotic stress. *BMC Genomics* **22**, 317, doi:10.1186/s12864-021-07633-y (2021).

19 Tascon, I. *et al.* Structural basis of proton-coupled potassium transport in the KUP family. *Nat Commun* **11**, 626, doi:10.1038/s41467-020-14441-7 (2020).

20 Shi, Y. Common folds and transport mechanisms of secondary active transporters. *Annu Rev Biophys* **42**, 51-72, doi:10.1146/annurev-biophys-083012-130429 (2013).

21 Licht, J. A., Berry, S. P., Gutierrez, M. A. & Gaudet, R. They all rock: A systematic comparison of conformational movements in LeuT-fold transporters. *Structure* **32**, 1528-1543.e1523, doi:https://doi.org/10.1016/j.str.2024.06.015 (2024).

22 Vastermark, A., Wollwage, S., Houle, M. E., Rio, R. & Saier Jr., M. H. Expansion of the APC superfamily of secondary carriers. *Proteins: Structure, Function, and Bioinformatics* **82**, 2797-2811, doi:https://doi.org/10.1002/prot.24643 (2014).

23 del Alamo, D., Meiler, J. & McHaourab, H. S. Principles of Alternating Access in LeuT-fold Transporters: Commonalities and Divergences. *Journal of Molecular Biology* **434**, 167746, doi:https://doi.org/10.1016/j.jmb.2022.167746 (2022).

24 Jegla, T., Busey, G. & Assmann, S. M. Evolution and Structural Characteristics of Plant Voltage-Gated K^+ Channels. *Plant Cell* **30**, 2898-2909, doi:10.1105/tpc.18.00523 (2018).

25 Yuan, G. *et al.* Research progress on plant shaker K+ channels. *Plants* **13**, 1423 (2024).

26 Alemán, F. *et al.* The F130S point mutation in the Arabidopsis high-affinity K^+ transporter AtHAK5 increases K^+ over Na^+ and Cs^+ selectivity and confers Na^+ and Cs^+ tolerance to yeast under heterologous expression. *Frontiers in Plant Science* **5**, doi:10.3389/fpls.2014.00430 (2014).

27 Jiménez-Estévez, E. *et al.* Increased tolerance to low K+, and to cationic stress of Arabidopsis plants by expressing the F130S mutant version of the K+ transporter AtHAK5. *Plant Physiology and Biochemistry* **212**, doi:10.1016/j.plaphy.2024.108768 (2024).

28 Qin, Y. J., Wu, W. H. & Wang, Y. ZmHAK5 and ZmHAK1 function in K^+ uptake and distribution in maize under low K^+ conditions. *J Integr Plant Biol* **61**, 691-705, doi:10.1111/jipb.12756 (2019).

29 Pilot, G., Gaymard, F., Mouline, K., Chérel, I. & Sentenac, H. Regulated expression of *Arabidopsis* Shaker K^+ channel genes involved in K^+ uptake and distribution in the plant. *Plant molecular biology* **51**, 773-787, doi:10.1023/A:1022597102282 (2003).

30 Lebaudy, A., Very, A. A. & Sentenac, H. K^+ channel activity in plants: genes, regulations and functions. *FEBS Lett* **581**, 2357-2366, doi:10.1016/j.febslet.2007.03.058 (2007).

31 Sardans, J. & Penuelas, J. Potassium Control of Plant Functions: Ecological and Agricultural Implications. *Plants (Basel)* **10**, doi:10.3390/plants10020419 (2021).

32 Tyerman, S. D. *et al.* in *New Phytologist.*1 edn 25-29 (Blackwell Publishing Ltd, 30488600).

33 Shah, I. H. *et al.* Exploring the role of nitrogen and potassium in photosynthesis implications for sugar: Accumulation and translocation in horticultural crops. *Scientia Horticulturae* **327**, doi:10.1016/j.scienta.2023.112832 (2024).

34 Rubio, F., Guillermo, E. & Rodríguez-Navarro, A. Cloning of Arabidopsis and barley cDNAs encoding HAK potassium transporters in root and shoot cells. *Physiologia Plantarum* **109**, 34-43, doi:10.1034/j.1399-3054.2000.100106.x (2000).

35 Zhao, Y., Liang, S., Huang, K. & Huang, R. Construction of a set of secreting expression vectors for Saccharomyces cerevisiea. *Wei Sheng Wu Xue Bao* **42**, 431-435 (2002).

36 Wright, M. B. *et al.* Potassium transport by amino acid permeases in Saccharomyces cerevisiae. *J Biol Chem* **272**, 13647-13652, doi:10.1074/jbc.272.21.13647 (1997).

37 Hopp, T. P. *et al.* A Short Polypeptide Marker Sequence Useful for Recombinant Protein Identification and Purification. *Bio/Technology* **6**, 1204-1210, doi:10.1038/nbt1088-1204 (1988).

38 Chalfie, M., Tu, Y., Euskirchen, G., Ward, W. W. & Prasher, D. C. Green fluorescent protein as a marker for gene expression. *Science* **263**, 802-805, doi:10.1126/science.8303295 (1994).

39 Niwa, H., Yamamura, K. & Miyazaki, J. Efficient selection for high-expression transfectants with a novel eukaryotic vector. *Gene* **108**, 193-199, doi:10.1016/0378-1119(91)90434-d (1991).

40 Lin, Y. C. *et al.* Genome dynamics of the human embryonic kidney 293 lineage in response to cell biology manipulations. *Nat Commun* **5**, 4767, doi:10.1038/ncomms5767 (2014).

41 Wang, X. *et al.* Structural insights into ion selectivity and transport mechanisms of Oryza sativa HKT2;1 and HKT2;2/1 transporters. *Nature Plants* **10**, 633-644, doi:10.1038/s41477-024-01665-4 (2024).

42 Lei, J. & Frank, J. Automated acquisition of cryo-electron micrographs for single particle reconstruction on an FEI Tecnai electron microscope. *Journal of Structural Biology* **150**, 69-80, doi:https://doi.org/10.1016/j.jsb.2005.01.002 (2005).

43 Zheng, S. Q. *et al.* MotionCor2: anisotropic correction of beam-induced motion for improved cryo-electron microscopy. *Nature Methods* **14**, 331-332, doi:10.1038/nmeth.4193 (2017).

44 Grant, T. & Grigorieff, N. Measuring the optimal exposure for single particle cryo-EM using a 2.6 Å reconstruction of rotavirus VP6. *eLife* **4**, e06980, doi:10.7554/eLife.06980 (2015).

45 Zhang, K. Gctf: Real-time CTF determination and correction. *Journal of Structural Biology* **193**, 1-12, doi:https://doi.org/10.1016/j.jsb.2015.11.003 (2016).

46 Punjani, A., Rubinstein, J. L., Fleet, D. J. & Brubaker, M. A. cryoSPARC: algorithms for rapid unsupervised cryo-EM structure determination. *Nature Methods* **14**, 290-296, doi:10.1038/nmeth.4169 (2017).

47 Punjani, A., Zhang, H. & Fleet, D. J. Non-uniform refinement: adaptive regularization improves single-particle cryo-EM reconstruction. *Nature Methods* **17**, 1214-1221, doi:10.1038/s41592-020-00990-8 (2020).

48 Chen, S. *et al.* High-resolution noise substitution to measure overfitting and validate resolution in 3D structure determination by single particle electron cryomicroscopy. *Ultramicroscopy* **135**, 24-35, doi:https://doi.org/10.1016/j.ultramic.2013.06.004 (2013).

49 Pettersen, E. F. *et al.* UCSF Chimera--a visualization system for exploratory research and analysis. *J Comput Chem* **25**, 1605-1612, doi:10.1002/jcc.20084 (2004).

50 Emsley, P., Lohkamp, B., Scott, W. G. & Cowtan, K. Features and development of Coot. *Acta Crystallogr D Biol Crystallogr* **66**, 486-501, doi:10.1107/s0907444910007493 (2010).

51 Adams, P. D. *et al.* PHENIX: a comprehensive Python-based system for macromolecular structure solution. *Acta Crystallogr D Biol Crystallogr* **66**, 213-221, doi:10.1107/s0907444909052925 (2010).

Methods

Yeast complementation assay

Wild-type (WT) and mutant AtHAK5[34] variants were cloned into the pYES2.0 yeast expression vector[35] (YouBio, China). Subsequently, the recombinant plasmids were transformed into a potassium-deficient Saccharomyces cerevisiae strain, CY162 (MATα ura3-52 leu2 trk1 Δ his3Δ200 his4-15 trk2Δ1::pCK64, synonymous with R5421)[36] (Shanghai Weidi Biotechnology Co., Ltd. China). Transformants were selected on SD-URA solid medium (containing 50 mM KCl; TaKaRa) and cultured at 30℃ for 48 h. Single colonies were verified by PCR and inoculated into SD-URA liquid medium, and grown overnight at 30°C. Then the yeast cells were collected and repeatedly washed with sterile water to remove residual potassium from the culture medium. The cells were adjusted to OD_{600} = 1.5 and diluted 1:10 into 4 gradients, out of which 5 uL were spotted onto AP agar (Coolaber, China) containing defined K^+ concentrations. The plates were inverted and cultured at 30 °C for 72 h before the final growth results were checked.

Cloning, expression, and purification of AtHAK5

The full-length coding sequence of the Arabidopsis thaliana HAK5 (UniProt ID: Q9M7K4) gene (NCBI Reference Sequence: NM_117416.3) was codon-optimized for mammalian expression and custom-synthesized by PCR. Confirmed by sequencing(Beijing Tsingke Biotech Co.), this optimized HAK5 sequence was engineered to include a C-terminal fusion of Flag and GFP tags and cloned into the pCAG expression vector[37-39]. For recombinant protein production, HEK293F cells (Thermo Fisher Scientific) were maintained in SMM-293TII medium (Sino Biological Inc.) at 37°C under 5% CO_2 with continuous agitation at

150 rpm in a ZCZY-CS9 shaker (Zhichu Instrument Co.)[40]. Plasmid DNA was transfected into HEK293F cells at a density of 2.0 × 10^6 cells/mL using linear polyethylenimine (PEI, Polysciences) as the transfection reagent. After 48 hours of incubation, cells were harvested by centrifugation at 4,000 g for 10 min, washed once with phosphate-buffered saline (PBS, pH 7.4), flash-frozen in liquid nitrogen, and stored at −80°C for downstream processing. For the purification of the HAK5, cell pellets were resuspended in lysis buffer [20 mM HEPES (pH 7.0), 150 mM NaCl, 1 mM KCl, 1% (w/w) DDM:CHS (10:1 ratio), 10 mM $MgCl_2$, 1 μM leupeptin, 1 μM pepstatin A, 1 μg/mL aprotinin, 1 mM PMSF, and 0.02 mg/mL DNase] and rotated continuously at 4°C for 2 h[41]. Lysates were clarified by centrifugation at 14,000 × g for 1 h, and the supernatant was incubated with Anti-DYKDDDDK G1 Affinity Resin (GenScript) for FLAG-tagged HAK5 capture. Bound protein was eluted using FLAG peptide, concentrated using an Amicon Ultra-4 centrifugal filter (100 kDa MWCO; Millipore), and further purified by size exclusion chromatography (SEC) on a Superose 6 Increase column (GE Healthcare). Peak fractions were pooled, concentrated to >15 mg/mL, and used for cryo-EM grid preparation.

Cryo-EM sample preparation and data acquisition

For cryo-EM specimen preparation, 3 μL of purified HAK5 protein was applied to glow-discharged holey carbon grids (Quantifoil Au R1.2/1.3) using a Vitrobot Mark IV (Thermo Fisher Scientific) with a 3-s blotting time. The grids were then loaded on a 300 kV Titan Krios electron microscope (Thermo Fisher Scientific Inc.) fitted with a K3 Summit direct electron detector (Gatan) and a GIF Quantum energy filter for optimal image acquisition. Images were acquired in super-resolution mode utilizing the AutoEMation software suite[42],

operating at a nominal magnification of 81,000× with an energy slit width set to 20 eV on the GIF Quantum energy filter. The defocus range was set from -1.2 μm to -2.2 μm to optimize image contrast. Each image stack was exposed to 2.56 s, with individual frame exposures of 0.08 s, culminating in 32 frames per stack. The cumulative dose per stack was controlled to approximately 50 e-/Å^2 to minimize radiation damage. Post-acquisition, the image stacks were subjected to motion correction using MotionCor2[43], and binned 2 fold, which yielded a final pixel size of 1.0773 (1.087/0.92) Å/pixel. Concurrently, dose weighting was applied to enhance image quality[44]. The defocus values for each micrograph were estimated using Gctf[45].

Image processing

The first 5350 micrographs for the HAK5 were collected and subsequently imported into the cryoSPARC (v3.3.1) for analysis[46,47]. Particle picking was initiated using the Blob picker with parameters set for a minimum resolution of 160 Å (Dmin) and a maximum resolution of 240 Å (Dmax). Several rounds of 2D classification were employed to sort the 4,351,235 particles into distinct 2D classes, and 697,684 particles were selected and subjected to an ab initio reconstruction, homogeneous refinement and several rounds of heterogeneous refinement sequentially. Particles from the best class of the final round of heterogeneous refinement were subjected to non-uniform refinement which yielded a 2.77 Å map for HAK5.

Then the remaining 5051 micrographs were collected and imported. Utilizing the 2D classes with clear features from the preceding phase as template to do the Template Picker for the entire 10,401 micrographs. With the calculated high-resolution map as referenc, all

the particles underwent iterative rounds of non-uniform refinement and heterogeneous refinement, culminating a resolution of 2.75 Å. The introduction of symmetric C2 further improved the resolution to 2.66 Å. The resolution estimates were determined using the gold-standard Fourier shell correlation (FSC) criterion of 0.143[48], validated with high-resolution noise substitution.

Model building and structure refinement

The predicted model for AtHAK5 (AlphaFold Protein Structure Database ID: AF-Q9M7K4-F1) was docked into the final map of AtHAK5 in CHIMERA[49]. Every residue was manually checked and adjusted in COOT[50]. The chemical properties of amino acid residues were considered during model building.

The amino terminus (residues 1-55), TM2-3 linker (residues 161-166) and the farthest part of cytoplasmic domain (residues 655-715) are invisible; hence, they are not built in the models. Two K^+ ions were tentatively modeled for AtHAK5 with purification buffer considered. In addition, numerous water molecules were also built.

Structure refinement was performed using phenix.real_space_refine application in PHENIX[51] real space with secondary structure and geometry restraints. The over-fitting of the overall model was monitored by refining the model in one of the two independent maps from the gold-standard refinement approach and testing the refined model against the other map. Statistics of the map reconstruction and model refinement can be found in Table S1.

Data and code availability.

Atomic coordinates and EM maps have been deposited in the Protein Data Bank (http://www.rcsb.org) and the Electron Microscopy Data Bank (https://www.ebi.ac.uk/pdbe/emdb/), respectively.

Funding

This work was supported by the Ministry of Science and Technology (MOST) of the People's Republic of China (2024YFA0916903 to H.S.), the National Natural Science Foundation of China (3250110417 to X.W.), the Zhejiang Provincial Natural Science Foundation (DQ24C050001 to H.S.), the Zhejiang Key Laboratories Project (2024E10052 to H.S.), Westlake University, and the Westlake Education Foundation (to H.S.).

Acknowledgements

We thank the Cryo-EM Facility and the HPC Center of Westlake University for providing data collection and computation support, respectively.

Author contributions

The project was conceived by H.S. Molecular cloning, protein expression and purification, cryo-sample preparation, and electron micrography data collection were performed by C.W and X.W. Yeast complementation assay were performed by C.W. Y.Q and C.W. conducted the structure reconstruction and model building. All authors contributed to data analysis. The initial draft of the manuscript was written by C.W. and subsequently revised and finalized by H.S.

Declaration of interests

The authors declare no competing interests.

Figure 1

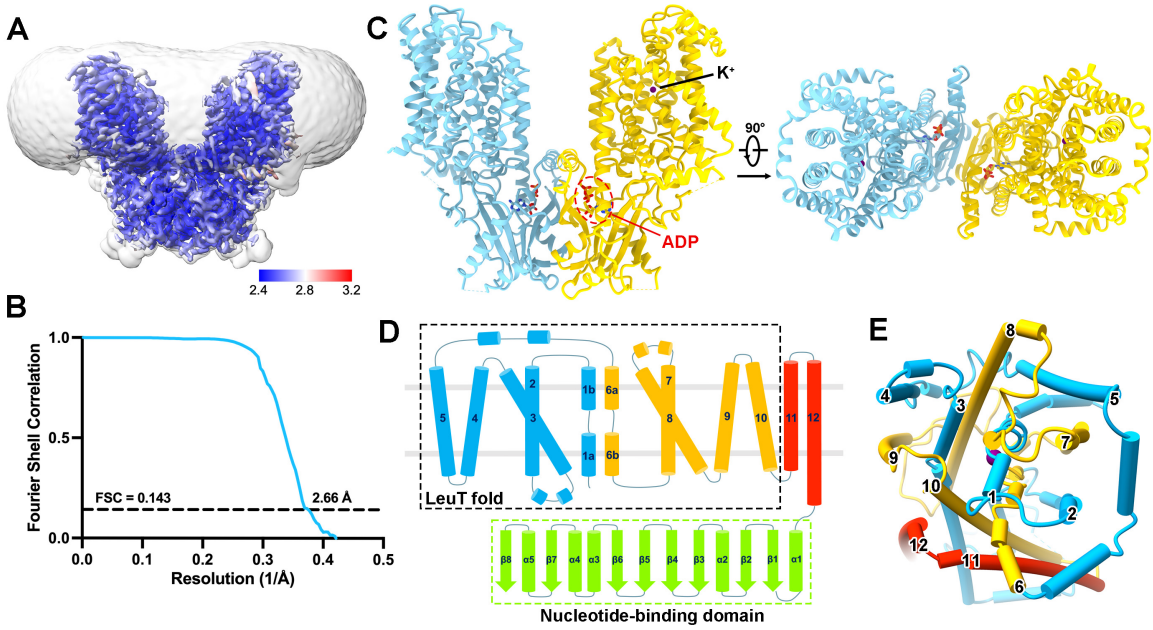

Figure 1. Structure determination and overall architecture of AtHAK5. (A) Cryo-EM density map of the AtHAK5 homodimer, colored by local resolution (Å) which was calculated using cryoSPARC. The figure was prepared in ChimeraX. **(B)** Gold-standard Fourier Shell Correlation (FSC) curve of the final 3D reconstruction, indicating a global resolution of 2.66 Å according to the 0.143 criterion. **(C)** Ribbon representation of the AtHAK5 homodimer, viewed from within the membrane plane (left) and from the extracellular side (right). The two protomers are colored cyan and yellow. Bound K^+ ions (purple spheres) and endogenous ADP molecules (shown as sticks) are indicated. Red dashed circles highlight the coordinated ADP. **(D)** Topology diagram of the AtHAK5 protomer. The transmembrane domain (helices 1–12) harbors a conserved LeuT-fold core (black dashed box, TMs 1–10). The extended intracellular C-terminus forms a novel adenine nucleotide-binding domain (NBD; green dashed box), comprising sequential α-helices and β-strands. **(E)** Top-down structural view of the transmembrane core from the

586 extracellular face. Helices are numbered. TMs 1, 3, 6, 8, and 10 intricately pack to form a

587 structural "knot" that intimately shapes the central K^+ permeation pathway.

588

Figure 2

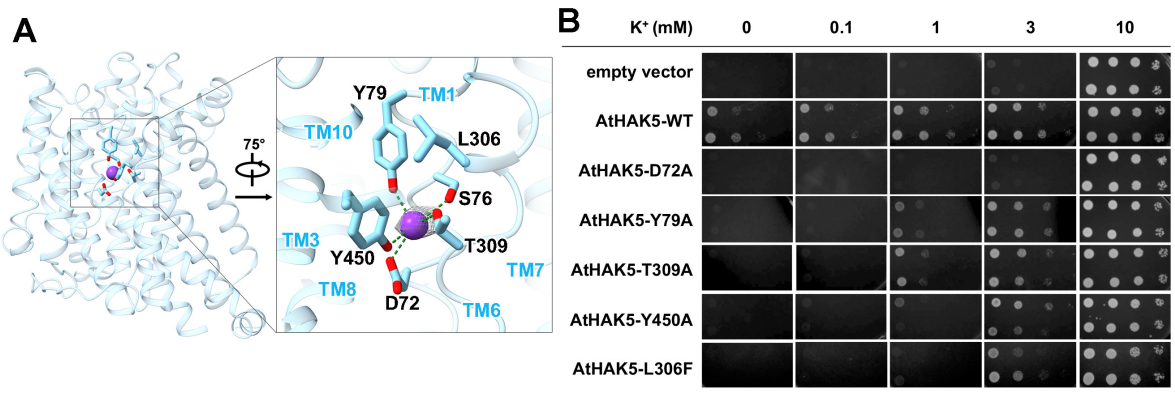

Figure 2. Structural basis and functional validation of high-affinity K^+ coordination in AtHAK5. (A) Overall ribbon representation of the AtHAK5 protomer (left) and a zoomed-in view detailing the central high-affinity K^+ binding pocket (right). The K^+ ion is depicted as a purple sphere, overlaid with its isolated cryo-EM density (gray mesh). The ion is rigidly coordinated by a network of polar and negatively charged residues, including D72, S76, and Y79 (TM1), T309 (TM6), and Y450 (TM10), with coordination bonds indicated by green dashed lines. The highly conserved L306 residue is positioned directly above the coordination sphere, putatively serving as an extracellular lid to gate ion entry. **(B)** *In vivo* functional validation of the K^+ coordination site via yeast complementation assay. The K^+-uptake deficient *Saccharomyces cerevisiae* strain CY162 was transformed with an empty vector, wild-type AtHAK5 (AtHAK5-WT), or the indicated single-point mutants targeting the coordination sphere (D72A, Y79A, T309A, Y450A) and the extracellular lid (L306F). Yeast cells were spotted onto solid media supplemented with varying concentrations of KCl (0 to 10 mM). Disruption of the primary coordination geometry or the L306F lid mutation severely impairs or abolishes yeast growth under strictly limiting K^+ concentrations (0.1–1 mM), confirming their crucial roles in high-affinity transport.

Figure 3

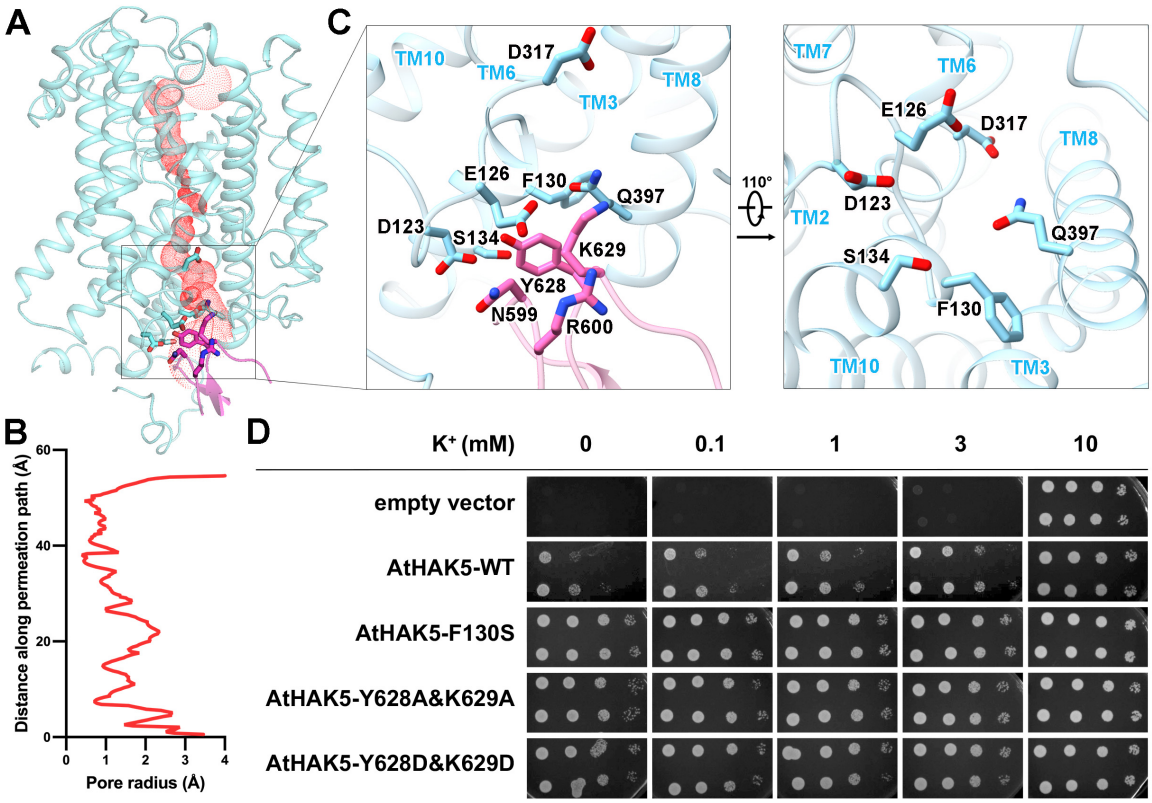

Figure 3. A cytoplasmic regulatory loop acts as an autoinhibitory plug at the intracellular exit of the K^+ permeation pathway. (A) Mapping of the central ion permeation pathway in AtHAK5. The pore volume (red stippled mesh) is visualized within the transmembrane core (cyan ribbon), illustrating a severe steric constriction at the intracellular (cytoplasmic) exit. **(B)** Pore radius profile along the central permeation axis. The radius drops significantly below 1 Å near the intracellular exit, confirming an occluded resting state that physically prevents K^+ release into the cytosol. **(C)** Close-up views of the intracellular exit gate. *Left*: A specific intracellular loop (ICL_{gate}, pink) projects directly into the cytoplasmic vestibule. Residues Y628 and K629 at the tip of the ICL_{gate} physically plug the pore by forming extensive interactions with a tightly packed cluster of exit-lining

619 residues (cyan sticks: D123, E126, F130, S134, and Q397). Residues N599 and R600 on an
620 adjacent cytosolic loop buttress and stabilize this occluded conformation. *Right*: A 110°-
621 rotated view with the ICL_{gate} omitted to clearly display the constricted exit bottleneck
622 formed by the TM helices. **(D)** *In vivo* yeast complementation assay demonstrating the
623 autoinhibitory function of the ICL_{gate}. Yeast cells (strain CY162) expressing wild-type
624 AtHAK5 (AtHAK5-WT) or the indicated mutants were grown on solid media containing 0
625 to 10 mM KCl. Targeted disruption of the physical plug (Y628A&K629A,
626 Y628D&K629D) or its key transmembrane interacting partner (F130S) effectively
627 uncouples the transporter from its native inhibition. This yields constitutively hyperactive
628 transport phenotypes that support robust yeast growth even under severe K^+ depletion (0
629 mM added K^+).
630

Figure 4

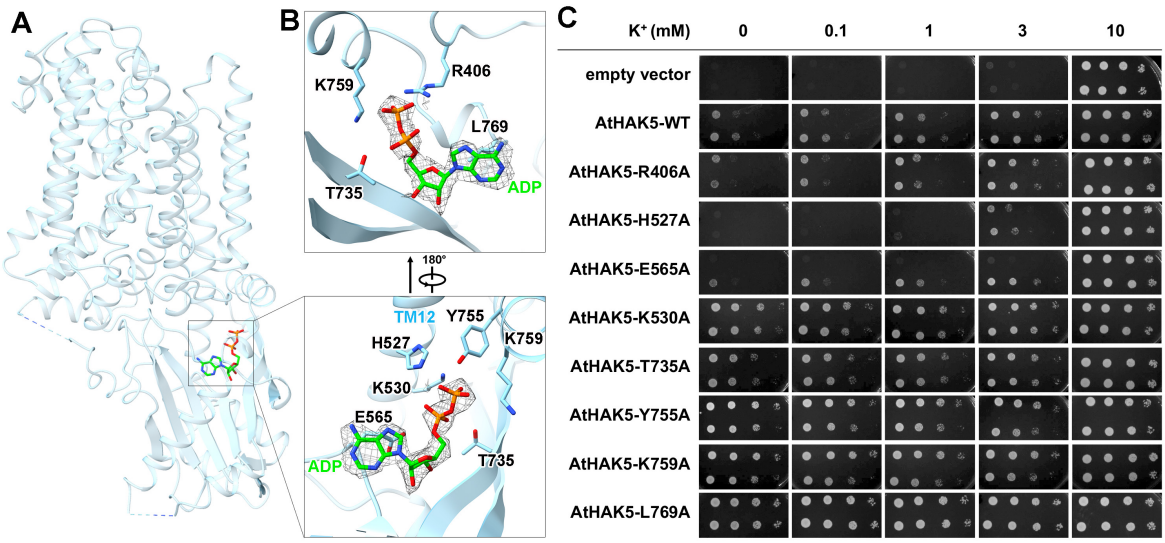

Figure 4. Structural and functional characterization of a novel cytoplasmic adenine nucleotide-binding domain (NBD) in AtHAK5. (A) Ribbon representation of the AtHAK5 protomer, highlighting the location of the massive, uniquely folded nucleotide-binding domain (NBD) at the cytoplasmic interface. An endogenous ADP molecule (green sticks) is deeply anchored within the domain. **(B)** Two orthogonal close-up views detailing the precise molecular architecture of the ADP-binding pocket. The bound endogenous ADP molecule is overlaid with its corresponding cryo-EM density map (gray mesh). The nucleotide is strictly coordinated by a network of highly conserved residues: positively charged residues (R406, K530, K759) tightly coordinate the α- and β-phosphates, while the negatively charged E565 residue anchors the adenine base. Additional spatial and polar stabilization is provided by H527, T735, Y755, and L769 (located near the extended TM12 helix). **(C)** *In vivo* yeast complementation assay demonstrating the profound regulatory role of the ADP-coordinating residues. Mutating the ADP-coordinating residues yields two strikingly divergent functional phenotypes across a K^+ concentration gradient (0 to 10 mM):

While mutations of R406A, H527A or E565A severely abrogates transport activity, mutations of K530A, T735A, Y755A, K759A or L769A yields constitutively hyperactive transport that supports robust yeast growth even under absolute K^+ starvation (0 mM added K^+).

652 **Figure 5**

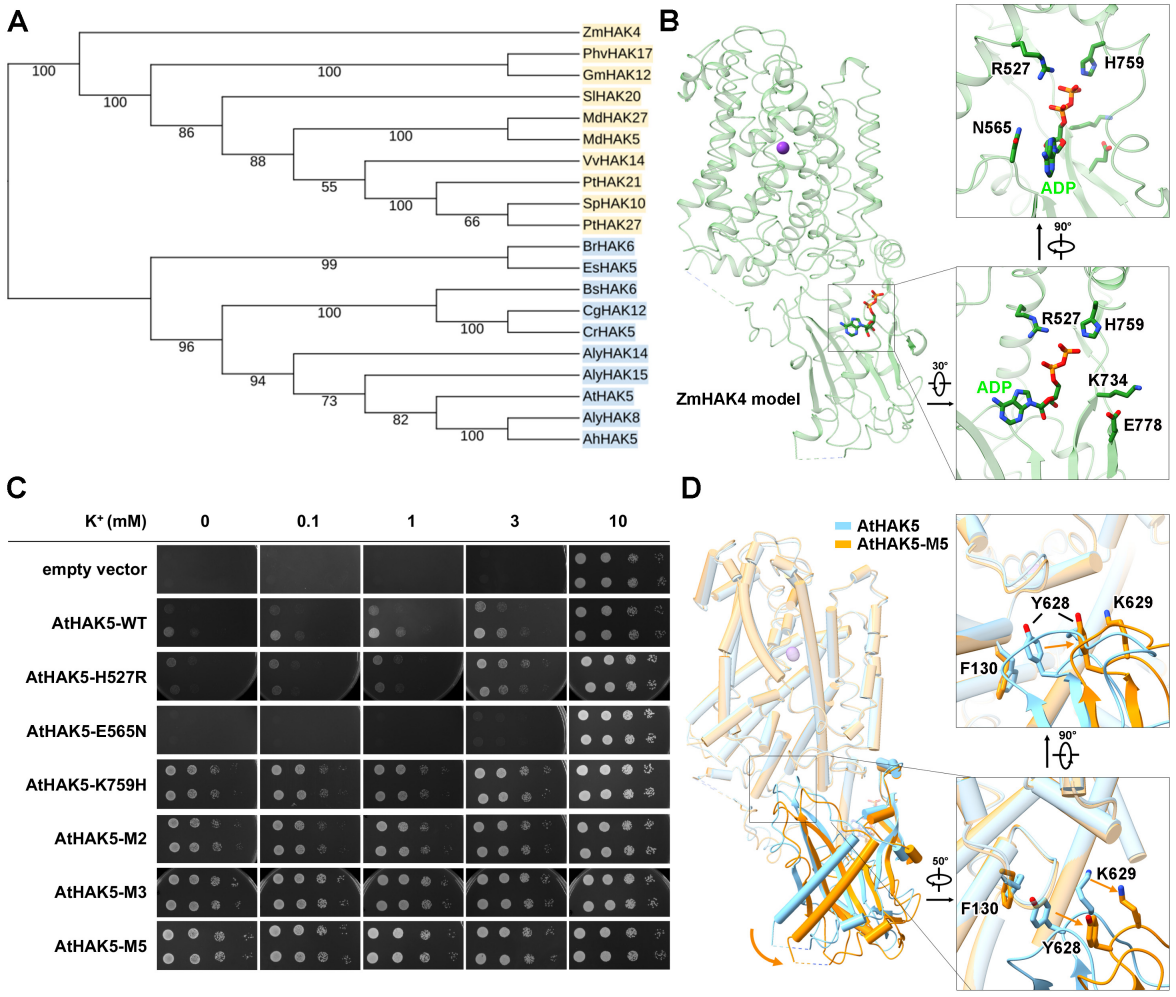

653

654 **Figure 5. The NBD structurally regulates the autoinhibitory ICL$_{gate}$. (A)** Phylogenetic
655 analysis of the nucleotide-binding domain (NBD) across diverse plant HAK homologs. The
656 tree delineates two distinct evolutionary clades defined by divergent nucleotide-
657 coordinating signatures. The first clade, represented by AtHAK5, and the second clade,
658 represented by ZmHAK4, feature distinct ADP-coordinating residues. **(B)** Structural model
659 of the ZmHAK4 protomer (green) and its predicted ADP-binding pocket. The insets detail
660 the natural sequence variations of the nucleotide-coordinating residues (labeled using
661 AtHAK5 numbering for direct comparison), illustrating an evolutionarily distinct structural

set-point for adenine nucleotide sensing. **(C)** *In vivo* yeast complementation assay evaluating AtHAK5 mutants rationally engineered to mimic the ZmHAK4 clade. Yeast cells (strain CY162) expressing WT AtHAK5 or the indicated mutants were grown across a K^+ concentration gradient. While the E565N single mutation abolishes function, the introduction of other ZmHAK4-like substitutions (H527R, K759H) and their combinations (M2, double mutant of H527R/K759H; M3, triple mutant of H527R/E565N/K759H; M5, quintuple mutant of H527R/E565N/E734K/K759H/K778E) strongly uncouples the transporter from its native autoinhibition. This generates constitutively hyperactive transport phenotypes supporting robust growth even under severe starvation (0 mM added K^+). **(D)** Structural basis of NBD-mediated transport gating. Superimposition of the autoinhibited AtHAK5-WT structure (cyan) and the uninhibited AtHAK5-M5 triple mutant structure (orange). Remodeling of the nucleotide pocket induces a massive rigid-body rotation of the entire cytoplasmic NBD toward the dimeric interface (indicated by the orange arrow). The detailed insets demonstrate that this domain swing acts as a mechanical lever, physically retracting the autoinhibitory ICL_{gate} (harboring Y628 and K629) away from the transmembrane pore exit (F130) to unplug the permeation pathway.

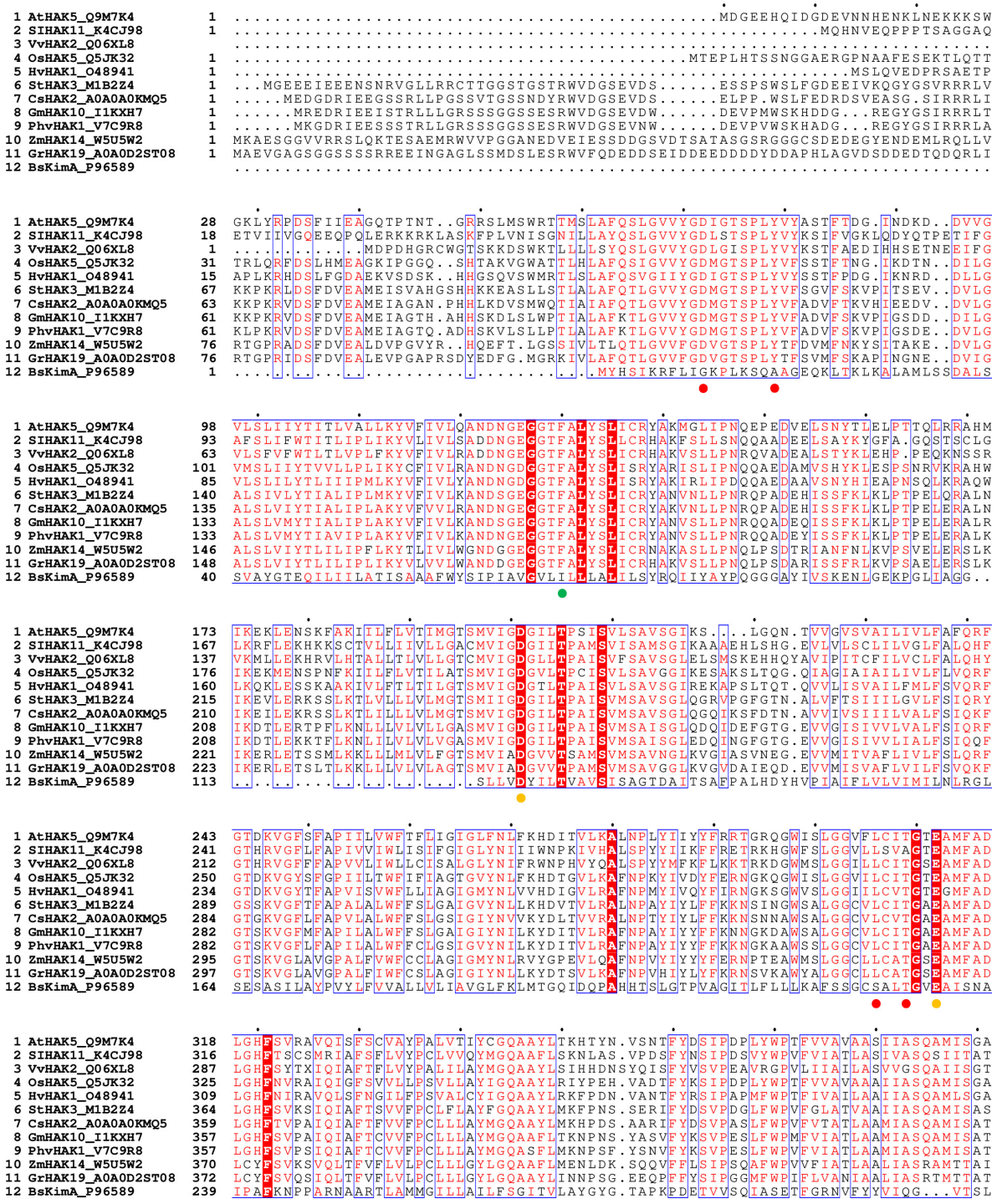

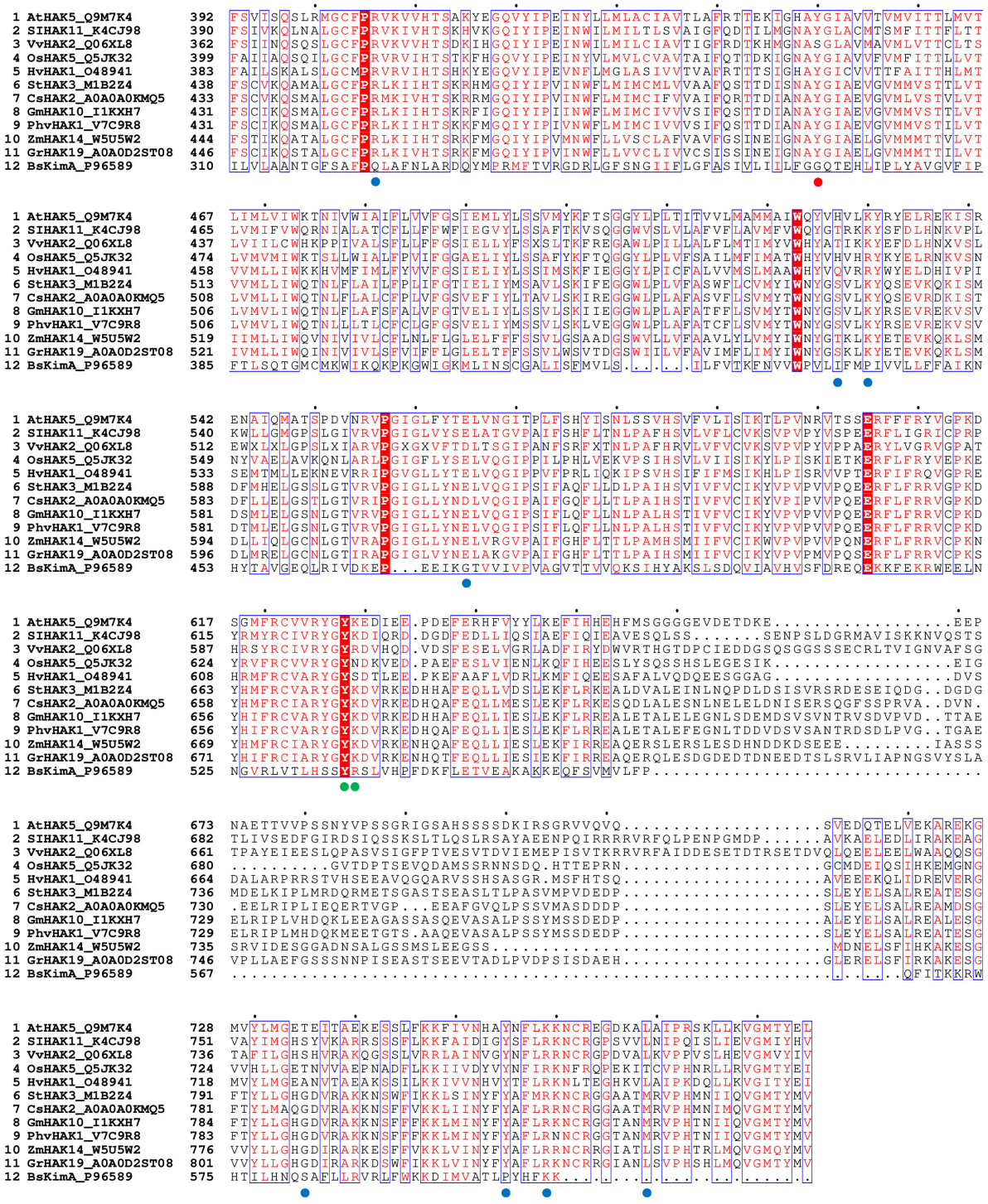

680

681 **Supplemental Figure S1. Sequence alignment of plant HAK and bacterial BsKimA**

682 **transporters.** The sequences of plant HAK and bacterial BsKimA transporters were

683 aligned using Clustal Omega and rendered with ENDscript 2. Invariant residues are

684 highlighted with a red background, while conserved residues are shown in red font.

685 Functional residues are indicated by colored circles below the alignment: K^+ coordination

686 (red), the permeation pathway exit (green), proton-coupling (orange), and ADP interactions

687 (blue).

688

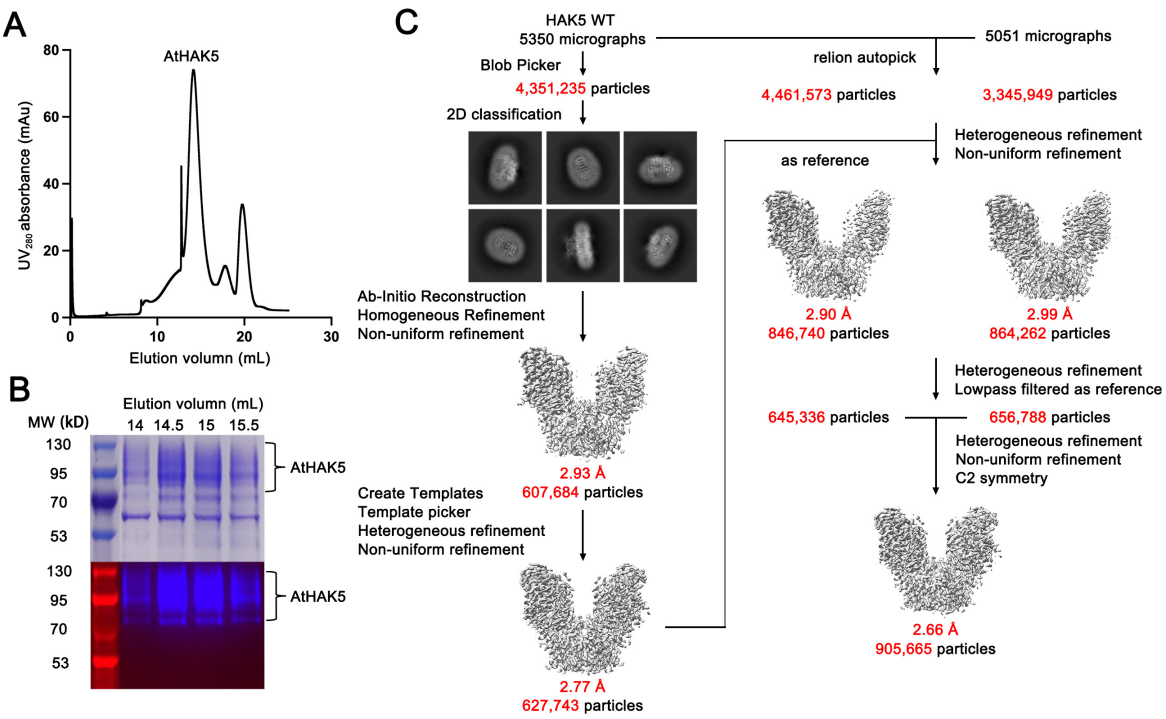

Supplemental Figure S2. Protein purification and flowchart for cryo-EM data processing of wild-type (WT) HAK5. (A, B) Size exclusion chromatography (SEC) elution profile of purified AtHAK5 **(A)** and the corresponding SDS-PAGE gel **(B)** visualized by coomassie-blue staining and fluorography. The peak fractions of SEC were pooled and concentrated for subsequent cryo-EM grid preparation. **(C)** Flowchart for cryo-EM data processing of WT HAK5. Please refer to the "Image processing" section in the Methods for details.

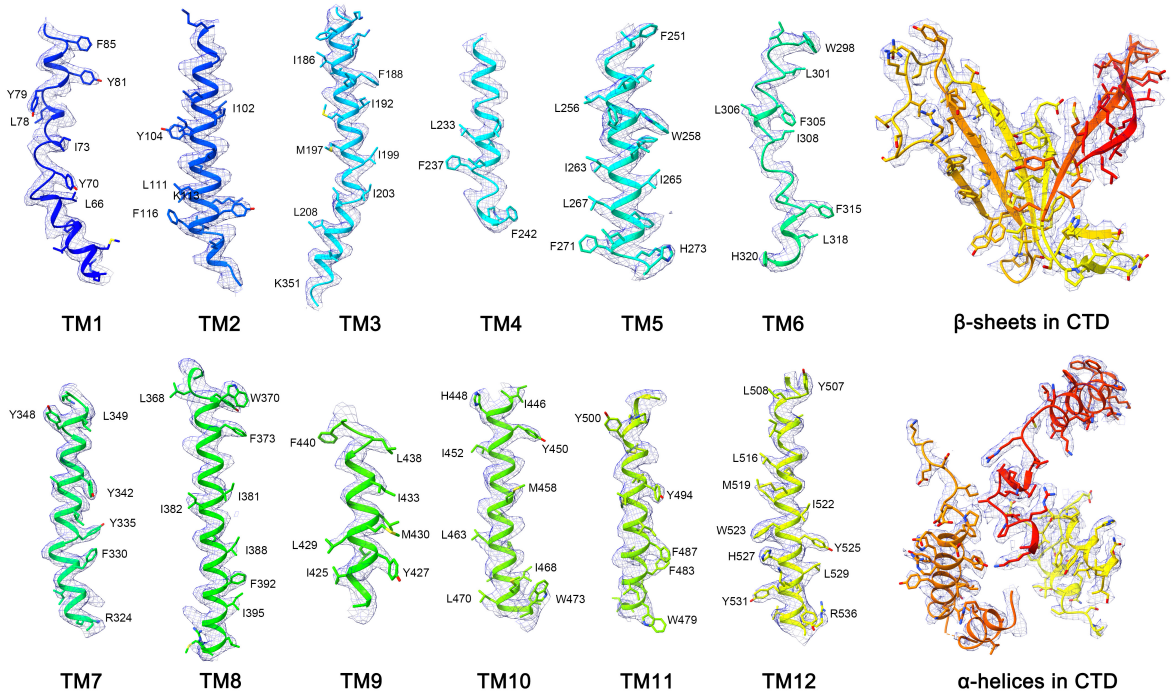

Supplemental Figure S3. EM densities for the transmembrane segments and the cytoplasmic domain of WT AtHAK5. The electron microscopy (EM) densities for the transmembrane segments and the cytoplasmic domain of AtHAK5 are visualized using UCSF ChimeraX. Residues with large side chains are labeled.

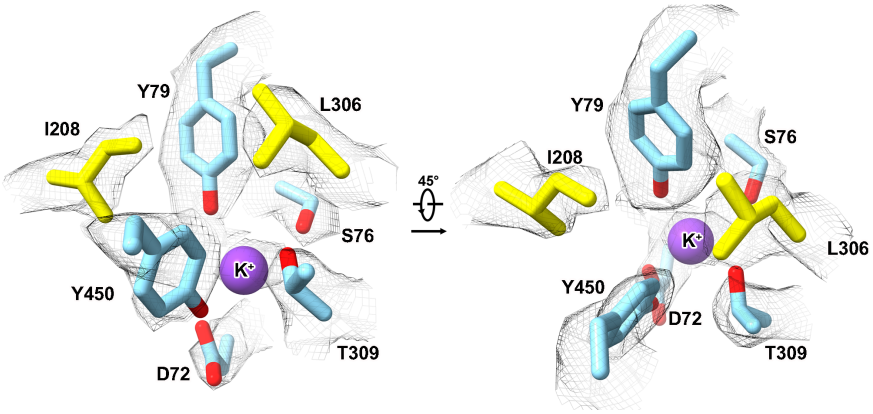

Supplemental Figure S4. EM densities for the K^+-coordinating residues in WT AtHAK5. The electron microscopy (EM) densities for K^+-coordinating residues are displayed in mesh using ChimeraX with two perpendicular views shown.

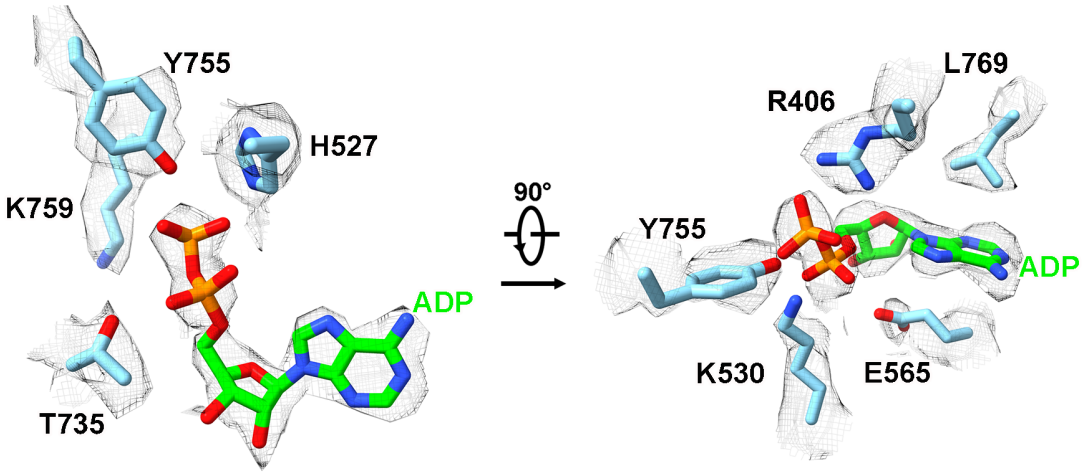

709

710 **Supplemental Figure S5. EM densities for the ADP interacting residues in WT**

711 **AtHAK5.** The electron microscopy (EM) densities for ADP binding residues are displayed

712 in mesh using ChimeraX with two perpendicular views shown.

713

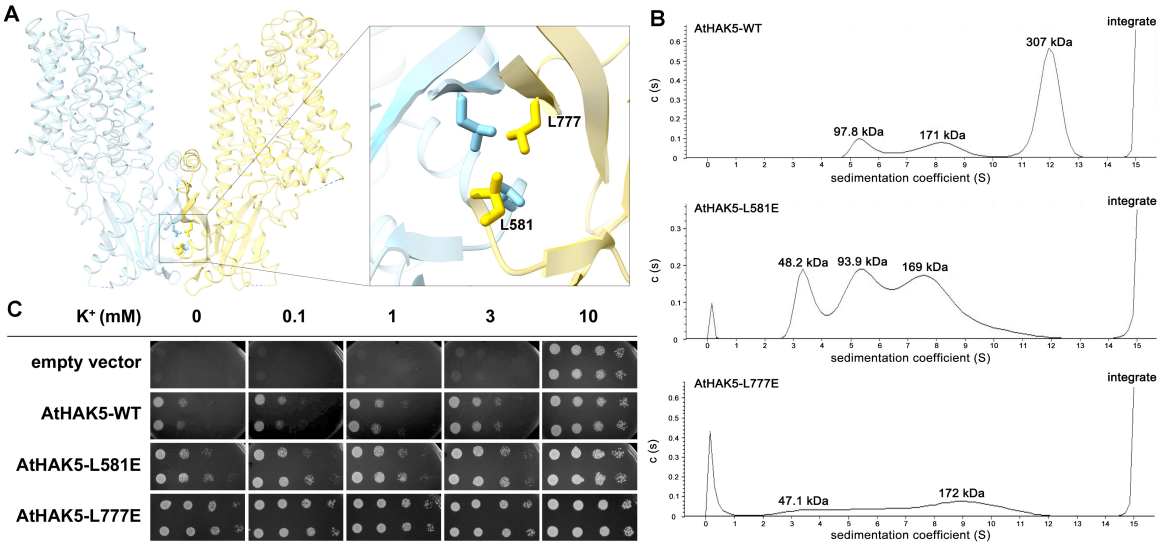

Supplemental Figure S6. Structural and biochemical characterization of the AtHAK5 dimeric interface. (A) Detailed structural view of the AtHAK5 homodimer interface. Key interacting residues, Leu581 and Leu777, are highlighted as sticks. The two protomers are colored blue and yellow, respectively. **(B)** Analytical ultracentrifugation (AUC) sedimentation profiles of wild-type (WT) AtHAK5 and the L581E and L777E mutants. The data biochemically confirm that these targeted single-point mutations successfully disrupt AtHAK5 homodimerization *in vitro*. **(C)** *In vivo* yeast complementation assay evaluating the functional impact of the dimer-disrupting mutations. The K^+-uptake-deficient yeast strain expressing WT AtHAK5 or the monomeric mutants (L581E and L777E) was grown on solid media under strictly limiting K^+ concentrations. Serial dilutions of the yeast cultures were plated in duplicate (parallel rows) for cross-validation. The robust growth of both mutants confirms that homodimerization is structurally dispensable for AtHAK5-mediated ion transport. Representative plates from three independent biological replicates are shown.

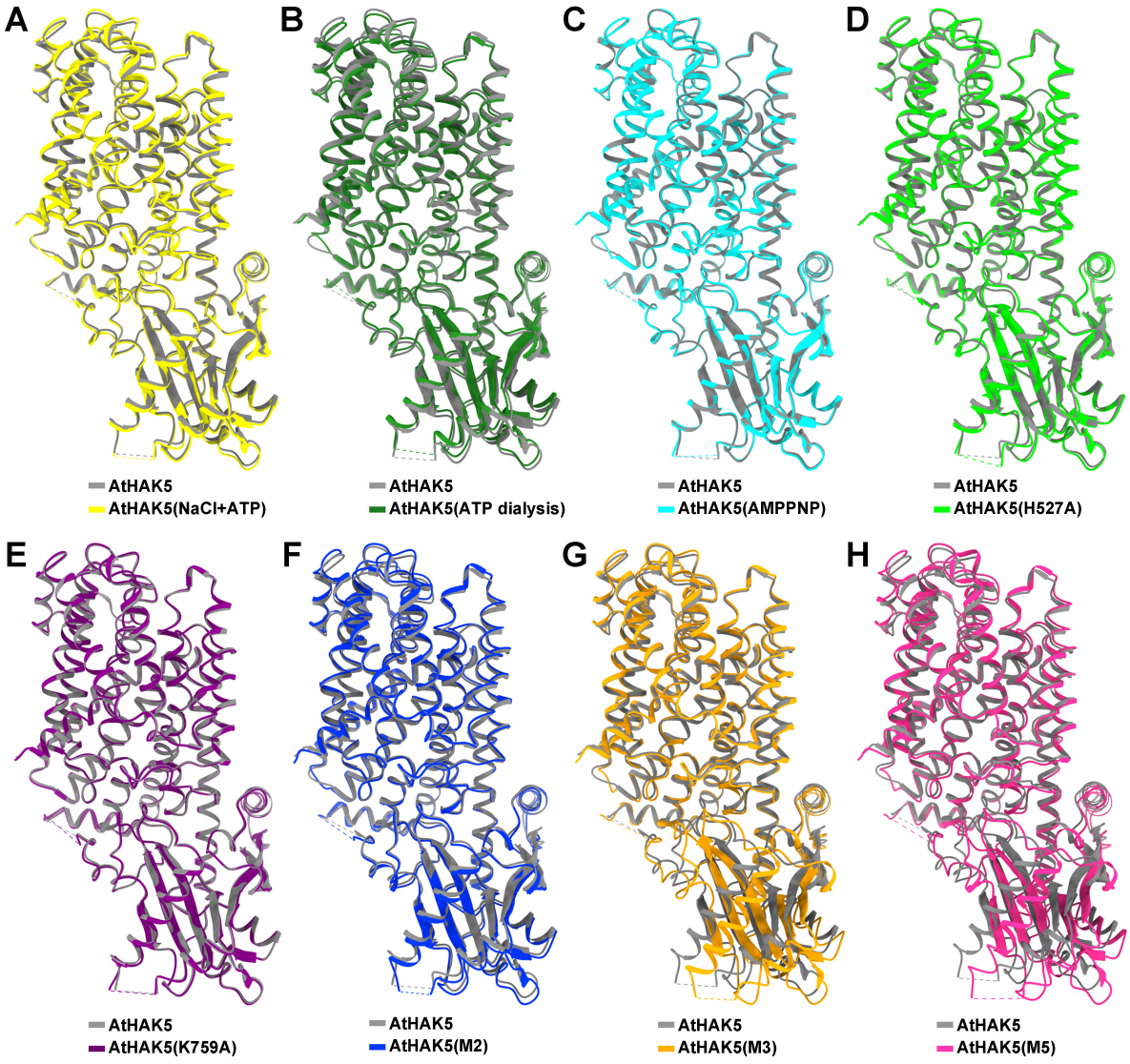

Supplemental Figure S7. Structural comparisons of AtHAK5 wild-type and rationally designed mutants under varying biochemical conditions. Superimposition of the autoinhibited wild-type (WT) AtHAK5 structure (reference state) with AtHAK5 structures determined under different biochemical treatments or harboring specific mutations. **(A)** AtHAK5 purified in the presence of NaCl and ATP. **(B)** AtHAK5 subjected to ATP dialysis. **(C)** AtHAK5 incubated with AMPPNP. **(D)** The activity-abrogating AtHAK5(H527A) mutant. **(E)** The constitutively active AtHAK5(K759A) mutant. **(F)** The rationally engineered double mutant AtHAK5(M2; H527R/K759H). **(G)** The rationally

engineered triple mutant AtHAK5(M3; H527R/E565N/K759H). **(H)** The rationally engineered quintuple mutant AtHAK5(M5; H527R/E565N/E734K/K759H/K778E). While panels **A–F** exhibit negligible global conformational changes compared to WT, panels **G** and **H** capture the profound rigid-body rearrangement of the NBD that unplugs the intracellular gate.

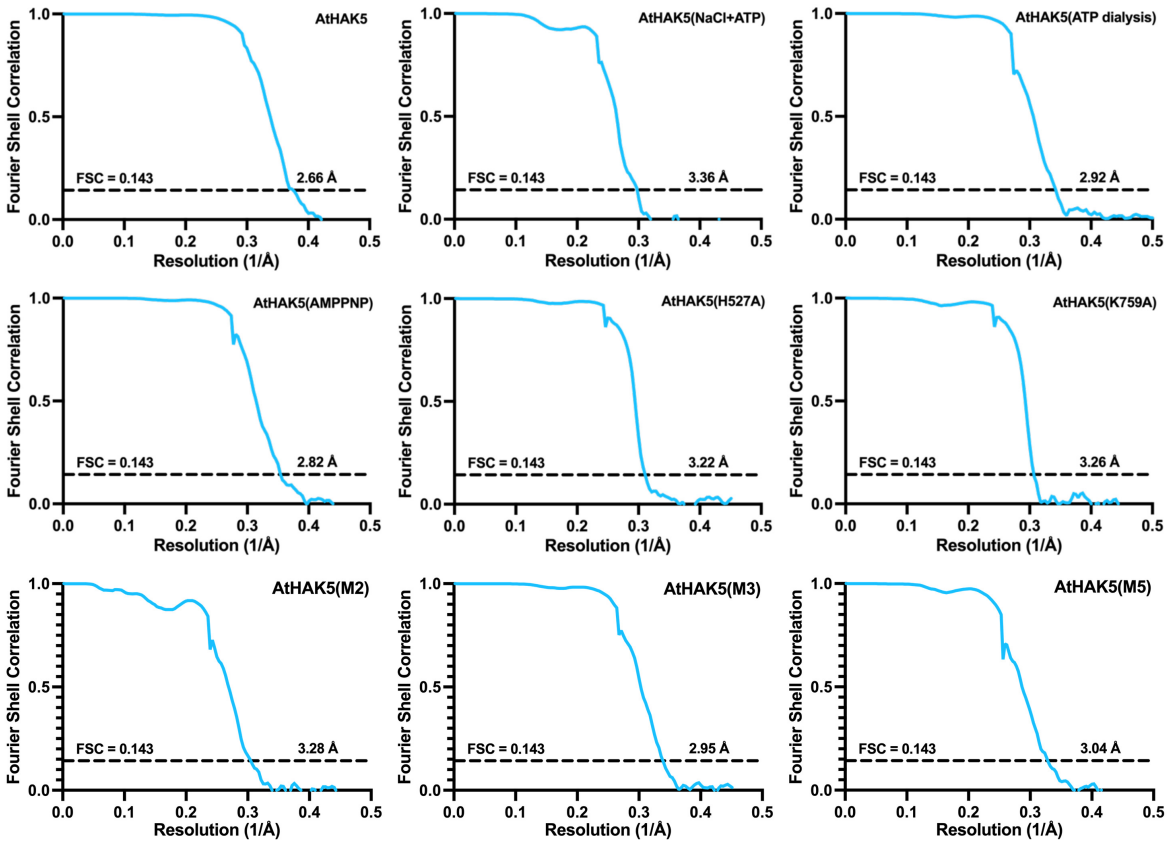

Supplemental Figure S8. Gold-standard Fourier shell correlation (FSC) curves for AtHAK5 cryo-EM reconstructions. The FSC curves demonstrate the overall resolution of the final 3D reconstructions for wild-type (WT) AtHAK5 and its various biochemical and mutational states, calculated using the 0.143 criterion. The corresponding global resolutions are as follows: WT AtHAK5 (2.66 Å); AtHAK5 purified in the presence of NaCl and ATP (3.36 Å); AtHAK5 subjected to extended ATP dialysis (2.92 Å); AtHAK5 incubated with 5 mM AMPPNP (2.82 Å); the H527A mutant (3.22 Å); the K759A mutant (3.26 Å); the rationally engineered double mutant M2 (3.28 Å); the rationally engineered triple mutant M3 (2.95 Å); and the rationally engineered quintuple mutant M5 (3.04 Å).

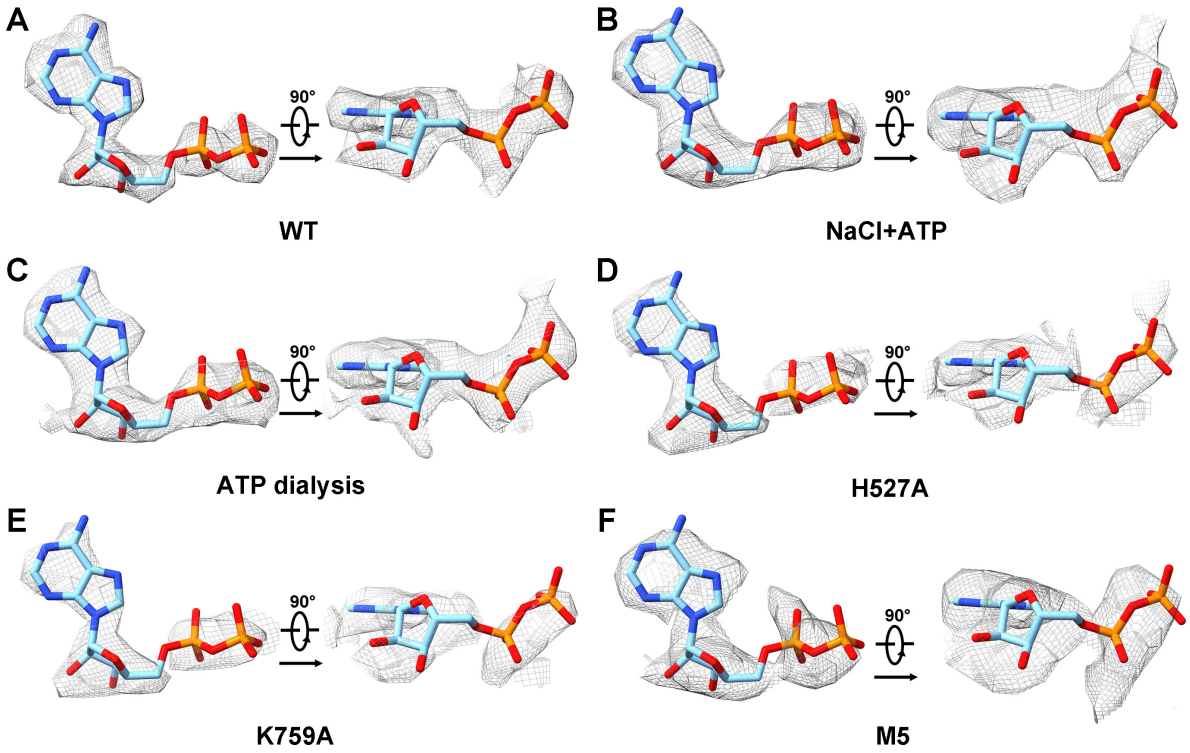

Supplemental Figure S9. Comparison of the ADP densities in AtHAK5 structures under different conditions or in ADP-interacting mutants. **(A)** ADP density in WT AtHAK5. **(B)** ADP density in AtHAK5 purified in the presence of NaCl and ATP. **(C)** ADP density in AtHAK5 suffered ATP dialysis. **(D)** ADP density in AtHAK5(H527A) mutant. **(E)** ADP density in AtHAK5(K759A) mutant. **(F)** ADP density in AtHAK5(M5) mutant.

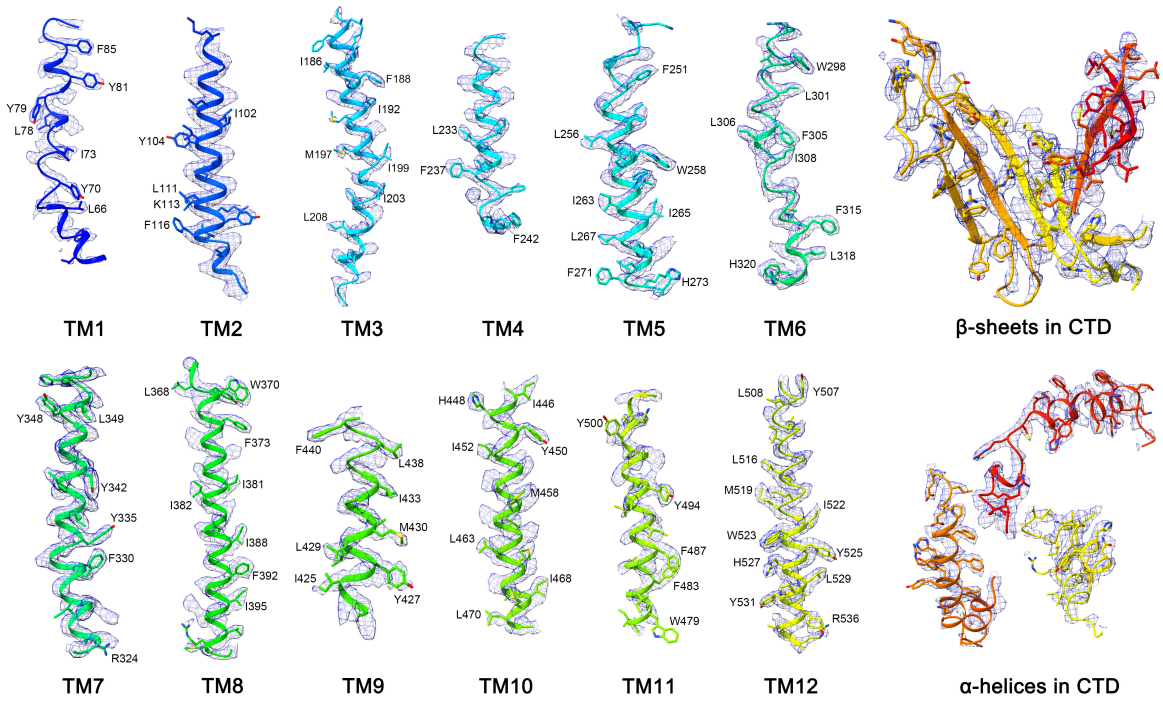

765

766 **Supplemental Figure S10. EM densities for the transmembrane segments and the**

767 **cytoplasmic domain of AtHAK5(M5).** The electron microscopy (EM) densities for the

768 transmembrane segments and the cytoplasmic domain of AtHAK5(M5) are visualized

769 using UCSF ChimeraX. Residues with large side chains are labeled.

770

Supplemental Table S1. Statistics for cryo-EM data collection and structural refinement.

Data collection	**AtHAK5**	**AtHAK5-NaCl +ATP**	**AtHAK5-ATP dialysis**	**AtHAK5-AMPPNP**	**AtHAK5-H527A**
EM equipment	Titan Krios (Thermo Fisher Scientific Inc.)				
Voltage (kV)	300				
Detector	Gatan K3 Summit				
Energy filter	Gatan GIF Quantum, 20 eV slit				
Pixel size (Å)	1.0773	1.087	0.92	1.0773	1.087
Electron dose ($e^-/Å^2$)	50				
Defocus range (μm)	-1.2~-2.2				
Number of collected movie stacks	10,401	2681	3213	3158	1582
Reconstruction					
Software	cryoSPARC v3.2, Relion 3.1				
Number of used particles	905,665	236,736	236,587	408,812	271,609
Symmetry	C2				
Overall resolution (Å)	2.66 Å	3.36 Å	2.92 Å	2.82 Å	3.22 Å
Map sharpening B-factor ($Å^2$)	-146.3	-195.5	-129.9	-144.2	-133.0
Refinement					
Software	Phenix				
Cell dimensions					
a=b=c (Å)	480				
α=β=γ (˚)	90				
Model composition					
Protein residues	1462				
Side chains assigned	1462				
K^+	2				
ADP	2				
H_2O	12	0	0	0	0
R.m.s deviations					
Bonds length (Å)	0.004	0.005	0.011	0.004	0.005
Bonds angle (˚)	0.672	0.657	0.885	0.703	0.679
Ramachandran plot statistics (%)					
Preferred	93.16	91.87	91.49	92.25	90.27
Allowed	6.69	8.13	8.05	7.60	9.73

Data collection	**AtHAK5-K759A**	**AtHAK5-M2**	**AtHAK5-M3**	**AtHAK5-M5**
EM equipment	Titan Krios (Thermo Fisher Scientific Inc.)			
Voltage (kV)	300			
Detector	Gatan K3 Summit			
Energy filter	Gatan GIF Quantum, 20 eV slit			
Pixel size (Å)	1.087			
Electron dose ($e^-/Å^2$)	50			
Defocus range (μm)	-1.2~-2.2			
Number of collected movie stacks	1539	3172	7193	4164
Reconstruction				
Software	cryoSPARC v3.2, Relion 3.1			
Number of used particles	236,347	236,736	749,243	129,025
Symmetry	C2			
Overall resolution (Å)	3.26 Å	3.28 Å	2.95 Å	3.04 Å
Map sharpening B-factor ($Å^2$)	-113.7	-150.9	-149.2	-104.2
Refinement				
Software	Phenix			
Cell dimensions				
a=b=c (Å)	480			
α=β=γ (˚)	90			
Model composition				
Protein residues	1462			
Side chains assigned	1462			
K^+	2			
ADP	2			
H_2O	0			
R.m.s deviations				
Bonds length (Å)	0.005	0.003	0.002	0.003
Bonds angle (˚)	0.694	0.782	0.637	0.651
Ramachandran plot statistics (%)				
Preferred	90.05	89.36	94.45	92.25
Allowed	9.95	10.26	4.94	7.67
Outlier	0.00	0.38	0.61	0.08